

Eckhaus-Benjamin-Feir Instability in Rotating Convection

Yuanming Liu and Robert E. Ecke

*Condensed Matter & Thermal Physics Group and Center for Nonlinear Studies, Los Alamos National Laboratory,
Los Alamos, New Mexico 87545*

(Received 19 March 1997)

We report experimental measurements of a traveling-wave state in rotating Rayleigh-Bénard convection. The fluid was water with a Prandtl number of 6.3 and a dimensionless rotation rate of 274. The marginal and Eckhaus-Benjamin-Feir stability boundaries were determined and the local amplitude and wave number were obtained from demodulation of shadowgraph images. The phase-diffusion coefficient and group velocity were measured in the stable wave number band. This system was found to be well described by the one-dimensional complex Ginzburg-Landau equation. [S0031-9007(97)03394-2]

PACS numbers: 47.20.Bp, 47.32.-y, 47.54.+r

The Ginzburg-Landau (GL) equation and its complex generalization, the complex GL (CGL) equation, are the generic model amplitude equations for pattern-forming systems, and a great deal of attention has been devoted to understanding their properties [1]. In effectively one-dimensional systems for steady patterns, detailed quantitative comparisons of experimental results and predictions of the GL equation have been made [2]. On the other hand, quantitative comparisons between *traveling-wave* systems and the CGL equation are much rarer. The only system for which there is both a mapping of experimental results onto the CGL equation, i.e., a determination of the CGL coefficients, and a study of the stability of traveling waves to long-wavelength perturbations is oscillatory convection in an annulus [3,4]. This work did not determine the stability boundary in any detail nor did it treat the phase dynamics in the stable region. The stability of traveling waves was investigated theoretically by Benjamin and Feir [5,6] and has many features of the Eckhaus instability in stationary patterns [7]. Other experimental systems that have exhibited features of the Eckhaus-Benjamin-Feir instability are binary-mixture convection [8,9] and traveling finger patterns [10] although neither could be fit quantitatively into the CGL framework. Because the CGL equation plays such a central role as a model for pattern-forming traveling-wave systems, it is important to establish its power to *quantitatively* predict properties for a real, physical experiment including the stability of traveling waves to the Eckhaus-Benjamin-Feir instability and extensions to a phase-equation description.

The traveling-wave sidewall mode [11–15] in rotating Rayleigh-Bénard convection provides an excellent experimental system for a detailed comparison with theoretical predictions derived from the one-dimensional CGL equation [12]. The sidewall mode travels in one direction because of the symmetry-breaking influence of rotation [16]. The bifurcation is forward and the wall mode is effectively one-dimensional in the azimuthal direction with periodic boundary conditions. A wide range of states with

discrete azimuthal wave number can be prepared, and detailed measurements using local probes and global optical shadowgraph are possible. Previously, the CGL coefficients for this system were determined using a cylindrical convection cell with a radius-to-height ratio $\Gamma = 2.5$ where R is the cell radius and d is the cell height. Here, we use a cell with $\Gamma = 5$ and are able to make much more extensive use of optical shadowgraph visualization because of the smaller cell depth. We have made quantitative measurements of the Eckhaus-Benjamin-Feir (EBF) instability in this system which compare very well with the theoretical predictions. We have also measured the phase-diffusion coefficient and nonlinear group velocity in the stable region. Excellent agreement is found between the behavior of this system and phenomena predicted from the CGL amplitude equation formalism. Discrepancies can be understood by considering higher-order terms in the amplitude equation.

The experimental apparatus is similar to the one used previously for studies of rotating convection [11,12]. In the new version, the whole apparatus including the shadowgraph optics was in the rotating frame. The convection cell consisted of an optically polished silicon bottom plate, a sapphire top plate, and a cylindrical Plexiglas sidewall. The cell height was $d = 1.000 \pm 0.005$ cm with a corresponding vertical thermal diffusion time $\tau_v = d^2/\kappa = 680$ sec (κ is the thermal diffusivity of the fluid). Each plate's average temperature was measured with a set of three thermistors equally spaced around the azimuth of the Plexiglas sidewall and in contact with the respective plate. Heat was supplied to the cell using a film heater on the bottom plate and the top-plate temperature was regulated at 24.1 °C with rms fluctuations of 0.0005 °C. The Prandtl number, ν/κ where ν is the kinematic viscosity of the fluid, for water at the cell mean temperature was 6.3. More details of the apparatus will be presented elsewhere.

The sidewall traveling wave is the first state that appears in rotating Rayleigh-Bénard convection as the temperature difference ΔT across the fluid layer is increased

provided the dimensionless rotation rate $2\pi fd^2/\nu$ (f is the rotation frequency) is greater than about 70. Above the critical temperature difference ΔT_c , there is an interval in ΔT in which the sidewall mode is the only convection state and above which the bulk state grows in the interior. The width of this interval increases with dimensionless rotation rate and for the value of 274 reported here the range of reduced bifurcation parameter $\epsilon \equiv \Delta T/\Delta T_c - 1$ is about 0.4. The transition to the traveling-wave convecting state is a supercritical Hopf bifurcation as determined by heat transport and local-temperature measurements, and different branches exist which correspond to states with different azimuthal mode number m [11,12]. The Nusselt number, the ratio of total heat transport to thermally diffusive heat transport, for the different branches is linear in ϵ with a common slope ($\pm 7\%$) and with ϵ^2 corrections of at most 3% at $\epsilon = 0.25$. The determination of the mode number was accomplished using optical shadowgraph imaging: an example image with $m = 23$ is shown in Fig. 1(a). The traveling-wave nature of the mode is seen in Fig. 1(b) which is an angle-time plot of a series of azimuthal signals constructed by averaging over a radial width of 3–4 pixels near the outer boundary. An additional probe of the wave dynamics is a thermistor embedded into the lateral wall which measures the local temperature of the thermal wave. This probe provides a highly accurate measurement of wave frequency Ω which varies linearly with ϵ with a finite value at onset. As opposed to the amplitude, the quadratic correction for the frequency is substantial, about 25% at $\epsilon = 0.25$.

To put these and further measurements into perspective, we now consider the theoretical framework for understanding nonlinear traveling waves of this type. To that end, we convert experimental quantities to dimensionless ones by normalizing space by the cell height d and time by the thermal diffusion time τ_ν . In particular, the dimensionless azimuthal wave number is defined as $k = 2\pi d/\lambda = m/\Gamma$ where λ is the azimuthal wave length $2\pi R/m$.

The generic envelope equation for pattern-forming nonlinear traveling waves is the CGL equation,

$$\tau_0(A_t + sA_x) = \epsilon(1 + ic_0)A + \xi_0^2(1 + ic_1)A_{xx} - g(1 + ic_3)|A|^2A, \quad (1)$$

where A is a complex amplitude which is assumed to be slowly varying in space and time relative to a fast carrier wave characterized by a frequency Ω and a wave number k . The fastest growing mode has Ω_c and k_c and one then defines small modulations about these critical values, $\omega = \Omega - \Omega_c$ and $q = k - k_c$. Substituting a spatially uniform traveling-wave solution of the form $A(x, t) = |A_0|\exp[i(qx + \omega t)]$ into Eq. (1) yields equations for the magnitude (real part) and the frequency (imaginary part): $\epsilon - \xi_0^2 q^2 = g|A_0|^2$ and $\tau_0(\omega + sq) = \epsilon c_0 - \xi_0^2 c_1 q^2 - gc_3|A_0|^2$. The equation for the magnitude gives the parabolic marginal stability boundary, $\epsilon_M = \xi_0^2 q^2$, and the square-root dependence of

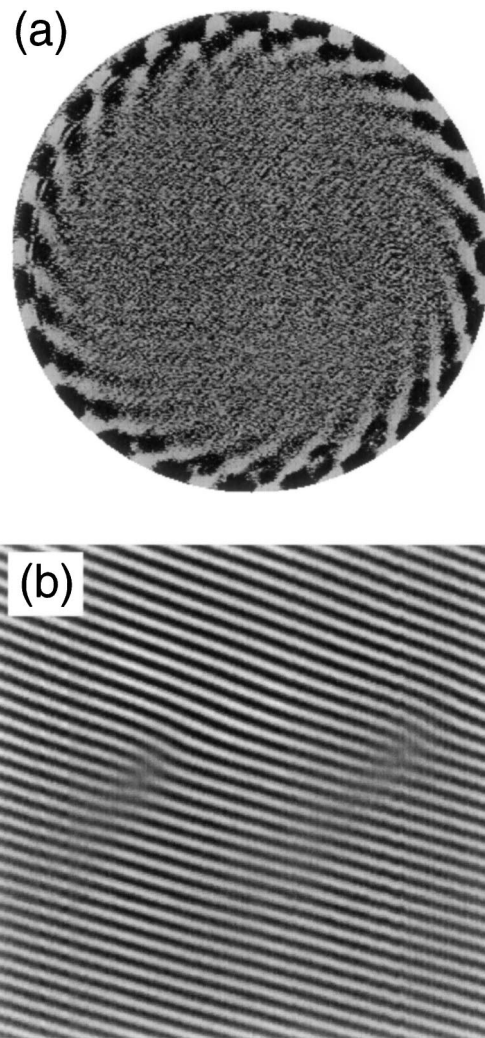


FIG. 1. Shadowgraph image of (a) traveling-wave wall state with $m = 23$ at $\epsilon = 0.19$ and (b) angle-time plot showing EBF instability. In (b) the horizontal axis is angle, with $\Delta\theta = \pi$, and the vertical axis is time (increasing upward) with $\Delta t = 5.0\tau_\nu$.

$|A_0| \sim (\epsilon - \epsilon_M)^{1/2}$. The frequency has a linear group velocity s , a term proportional to ϵ , a linear dispersive part proportional to q^2 , and the nonlinear dispersion proportional to $|A|^2$. We have determined by the methods described in [12] the following experimental values for the coefficients in Eq. (1): $\Omega_c = 21.95 \pm 0.05$, $k_c = 4.65 \pm 0.01$, $\tau_0 = 0.018 \pm 0.005$, $s = 2.65 \pm 0.05$, $\xi_0 = 0.179 \pm 0.004$, $g = 0.84 \pm 0.01$, $c_0 - c_1 = (5 \pm 1)\tau_0 = 0.08 \pm 0.03$, and $c_0 - c_3 = (20.4 \pm 0.4)\tau_0 = 0.37 \pm 0.07$. The differences between these coefficients and the ones determined previously [12] are attributable to their different dimensionless rotation rates [14]. It is necessary to use transient or modulation techniques to determine c_3 independently, and although our present measurements suggest $c_3 \ll c_0$ we do not have a precise value for c_3 . For evaluation purposes, we will use $c_0 = 0.42$, $c_1 = 0.34$, and $c_3 = 0.05$.

The EBF boundary in the space of ϵ and q was determined experimentally by preparing an m -mode state and quenching ΔT into the unstable region. A series of such quenches provided a time between the start of the jump and the appearance of a dislocation which signaled the creation or destruction of a roll pair. An example of this dislocation signature of the EBF instability is shown in the angle-time plot in Fig. 1(b). The time before appearance of a dislocation diverges as the EBF boundary is approached from below and linear extrapolation of several runs is adequate to determine the boundary quite accurately. The marginal stability boundary, determined from linear extrapolation of $|A_0|^2$ to zero for fixed q , and the EBF boundary are shown in Fig. 2. For comparison, the theoretical prediction for the EBF boundary, $\epsilon_E = \{[2(1 + c_3^2) + 1 + c_1 c_3]/(1 + c_1 c_3)\} \epsilon_M$, evaluated using the experimental coefficients with no free fitting parameters, is shown as a dashed line. The solid line is a fit to the marginal stability boundary ϵ_M which determines the coefficient ξ_0 . The agreement between experiment and theory is excellent. Note that the ratio ϵ_E/ϵ_M is 2.97, quite close to the pure Eckhaus value of 3.

The image of the traveling wave in Fig. 1 can be represented by the local amplitude and wave number k which is much closer to the theoretical CGL description. An interesting example of this representation is shown in the angle-time plot of Fig. 3. There is a periodic modulation of both fields with a spatial mode number of three leading up to the nucleation of two dislocations which takes the state from $m = 17$ to $m = 19$. The number of dislocations and the mode number of the pre-nucleation distortion varies between 1 and 6 and is most likely a measure of the most unstable phase distortion. After the dislocation nucleations there is another periodic distortion which slowly dies away. The presence of these periodic distortions leads us to consider the phase equation for the CGL equation. Long-wavelength phase modulations with wave number p are governed by a phase-diffusion equation of the form [4]

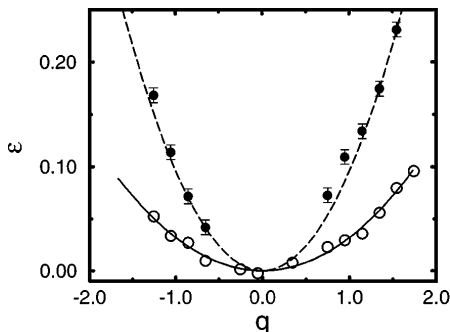


FIG. 2. Stability diagram for traveling waves at $\Omega = 274$ showing data for marginal stability (\circ) and EBF (\bullet) boundaries. Solid line is a parabolic fit to marginal stability data. Dashed line is prediction based on the CGL equation with experimentally determined coefficients.

$$\frac{\partial \phi}{\partial t} + v_g \frac{\partial \phi}{\partial x} = D \frac{\partial^2 \phi}{\partial x^2}, \quad (2)$$

where $D = (\xi_0^2/\tau_0)[1 + c_1 c_3 - 2\tilde{q}^2(1 + c_3^2)/(1 - \tilde{q}^2)]$ with $\tilde{q}^2 = \xi_0^2 q^2/\epsilon$ and $v_g = 2\xi_0^2(c_3 - c_1)q/\tau_0$. D is positive in the EBF stable region and goes to zero at the EBF boundary. This equation is also subject to periodic boundary conditions and thus there are only discrete values of p corresponding to mode numbers $n = 1, 2, \dots$, where $p = n/\Gamma$. A solution of the form $\phi \sim \exp\{i(px - rt) + \sigma t\}$ yields expressions for the frequency $r = pv_g$ and the growth rate $\sigma = -p^2 D$ of the phase modulation. Because of the p^2 dependence of the decay and the discrete nature of p , the only remaining wave number component after a short time corresponds to $n = 1$. Using the local probe, we have measured D and v_g for a range of q within the EBF stable band and for several different values of ϵ . In Fig. 4, a representative plot shows the frequency and magnitude of the signal at the probe for $\epsilon = 0.26$ after demodulation by the fast frequency at $q = 0.74$. The decay rate of the envelopes yields D and the oscillation frequency is proportional to v_g . The magnitude typically lags the frequency by about 0.5 radians, consistent with the approximation that the magnitude which relaxes on a time scale $\tau_0/\epsilon \approx 0.1$ is slaved to the phase which has a much longer decay rate of order 20. Figure 5 shows the values of D and v_g determined by assuming $p = 1/\Gamma = 0.2$. The solid and dashed curves in Fig. 5(a) show predictions of Eq. (2) for $\epsilon = 0.06$ and 0.12 , respectively, using the parameters listed earlier except with a modified value of $\tau_0 = 0.02$ which is within its specified error bars. The agreement is quite reasonable. For higher $\epsilon = 0.26$, the

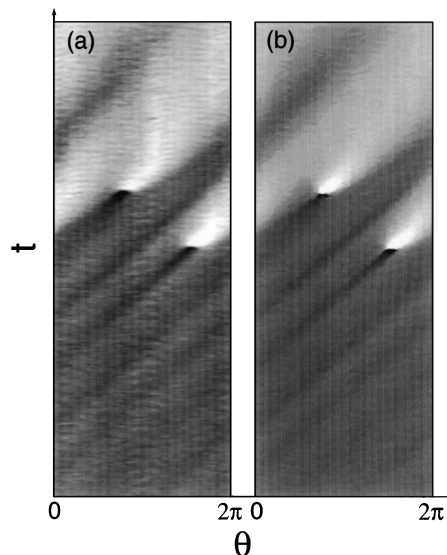


FIG. 3. Angle-time plots of (a) magnitude and (b) wave number showing two dislocation events which indicate an EBF transition from $m = 17$ to $m = 19$. Time increases upward. The gray-scale coding is dark for low magnitude (wave number) and white for high magnitude (wave number).

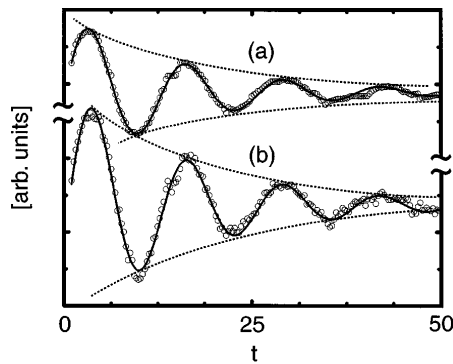


FIG. 4. Demodulated (a) frequency and (b) magnitude of the spatial modulation for $m = 27$ and $\epsilon = 0.26$. Solid (dashed) curves show fits to a decaying periodic function (envelope).

curve deviates substantially from an inverted parabola, similar to the case for the pure Eckhaus instability for steady patterns [2]. It is actually remarkable that the simple phase equation works so well given the restrictive limits under which it is derived [4]. The behavior of v_g illustrated in Fig. 5 shows rather large discrepancies with the simple theory which predicts ϵ independent values of $v_g|_{q=0} = s$ and of $dv_g/dq|_{q=0} = 2(c_3 - c_1)\xi_0^2/\tau_0$. Although the finite ϵ values of these quantities appear to converge to the $\epsilon = 0$ values shown in Fig. 5(b), the ϵ dependence of $v_g|_{q=0}$ is large and there is a big quadratic q dependence of v_g which is particularly noticeable for

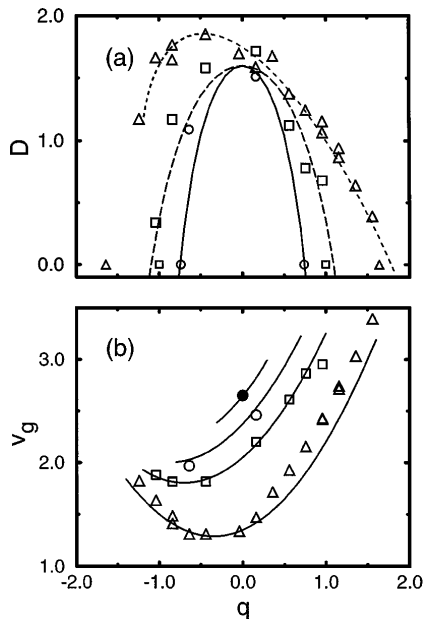


FIG. 5. (a) D vs q for $\epsilon = 0.26$ (Δ), $\epsilon = 0.12$ (\square), and $\epsilon = 0.06$ (\circ). Solid and long-dashed curves are fits consistent with CGL predictions and experimental parameters. Short dashed line is guide to eye for data with $\epsilon = 0.26$. Points with $D = 0$ are obtained from the EBF boundary shown in Fig. 2. (b) v_g vs q for same data as (a) with addition of $\epsilon = 0.0$ (\bullet). Solid lines are fits to data discussed in the text.

$\epsilon = 0.26$. These deviations suggest that higher-order corrections to the CGL amplitude equation are needed to describe the data more quantitatively.

The CGL equation is a perturbation expansion in powers of small quantities q and ϵ . Higher-order terms will be important at some level, depending on the nonuniversal values of the parameters multiplying those terms. In order to account for the behavior of v_g , we need to include third-order terms proportional to A_{xxx} and $A_x|A|^2$ and the fifth-order nonlinearity $|A|^4A$. The importance of the third-order derivative terms is not surprising since rotation breaks the $x \rightarrow -x$ symmetry which typically forbids them. The additional higher-order terms suggested here imply a form for the group velocity: $v_g = s + a_1\epsilon + a_2(1 - a_3\epsilon)q + a_4q^2$. The values $s = 2.65$, $a_1 = -5$, $a_2 = 1$, $a_3 = 2.5$, and $a_4 = 0.5$ yield the solid curves in Fig. 5. Although these corrections are important, the excellent agreement between the simple theory and the data indicates that the CGL equation yields a firm theoretical foundation for this system and sets the stage for a variety of further experiments and theoretical investigations.

We acknowledge useful discussions with G. Ahlers, R. Camassa, E. Knobloch, D. Prasad, and H. Riecke. This work was funded by the U.S. Department of Energy.

- [1] M. C. Cross and P. C. Hohenberg, *Rev. Mod. Phys.* **65**, 851 (1993).
- [2] G. Ahlers, in *Lectures in the Science of Complexity*, edited by D. Stein, SFI Studies in the Sciences of Complexity Vol. 1 (Addison Wesley, Redwood City, CA, 1989), p. 175.
- [3] V. Croquette and H. Williams, *Phys. Rev. A* **39**, 2765 (1989).
- [4] B. Jانياud, A. Pumir, D. Bensimon, V. Croquette, H. Richter, and L. Kramer, *Physica (Amsterdam)* **55D**, 269 (1992).
- [5] T. Benjamin and J. Feir, *J. Fluid Mech.* **27**, 417 (1967).
- [6] A. Newell, *Envelope Equations*, Lectures in Applied Mathematics Vol. 15 (American Mathematical Society, Providence, RI, 1974).
- [7] V. Eckhaus, *Studies in Nonlinear Stability Theory*, Springer Tracts in Natural Philosophy Vol. 6 (Springer-Verlag, Berlin, 1965).
- [8] P. Kolodner, *Phys. Rev. A* **46**, 1739 (1992); **46**, 6431 (1992).
- [9] G. Baxter, K. Eaton, and C. Surko, *Phys. Rev. A* **46**, 1735 (1992).
- [10] L. Pan and J. de Bruyn, *Phys. Rev. E* **49**, 2119 (1994).
- [11] F. Zhong, R. E. Ecke, and V. Steinberg, *Phys. Rev. Lett.* **67**, 2473 (1991); *J. Fluid Mech.* **249**, 135 (1993).
- [12] L. Ning and R. E. Ecke, *Phys. Rev. E* **47**, 3326 (1993).
- [13] H. Goldstein, E. Knobloch, I. Mercader, and M. Net, *J. Fluid Mech.* **248**, 583 (1993).
- [14] E. Kuo and M. C. Cross, *Phys. Rev. E* **47**, 2245 (1993).
- [15] J. Hermann and F. Busse, *J. Fluid Mech.* **255**, 183 (1993).
- [16] R. E. Ecke, F. Zhong, and E. Knobloch, *Europhys. Lett.* **19**, 177 (1992).